

Response of braiding channel morphodynamics to peak discharge changes in the Upper Yellow River

Filip Schuurman,^{1*} Wanquan Ta,² Sander Post,¹ Marius Sokolewicz,¹ Marcela Busnelli¹ and Maarten Kleinhans³

¹ Department of Rivers and Coasts, Royal HaskoningDHV, Amersfoort, The Netherlands

² Key Laboratory of Desert and Desertification, Cold and Arid Regions Environmental and Engineering Research Institute, Chinese Academy of Sciences, Lanzhou, China

³ Faculty of Geosciences, Department of Physical Geography, Utrecht University, Utrecht, The Netherlands

Received 13 July 2016; Revised 22 December 2017; Accepted 8 January 2018

*Correspondence to: Filip Schuurman, Department of Rivers and Coasts, Royal HaskoningDHV, Amersfoort, The Netherlands. E-mail: filip.schuurman@rhdhv.com

ESPL

Earth Surface Processes and Landforms

ABSTRACT: The braiding intensity and dynamics in large braiding rivers are well known to depend on peak discharges, but the response in braiding and channel–floodplain transformations to changes in discharge regime are poorly known. This modelling study addresses the morphodynamic effects of increasing annual peak discharges in braiding rivers. The study site is a braiding reach of the Upper Yellow River. We estimated the effects on the larger-scale channel pattern, and on the smaller-scale bars, channel branches and floodplains. Furthermore, we determined the sensitivity of the channel pattern to model input parameters. The results showed that the dominant effect of a higher peak discharge is the development of chute channels on the floodplains, formed by connecting head-cut channels and avulsive channels. Widening of the main channel by bank erosion was found to be less dominant. In addition, sedimentation on the bars and floodplains increased with increasing peak discharge. The model results also showed that the modelled channel pattern is especially sensitive to parametrization of the bed slope effect, whereas the effect of median grain size was found to be relatively small. Copyright © 2018 John Wiley & Sons, Ltd.

KEYWORDS: Yellow River; discharge regulation; Delft3D; braiding; floodplain

Introduction

Background

In the context of recent progress in numerical modelling of braided river morphodynamics (Schuurman *et al.*, 2013; Nicholas, 2013a; Yang *et al.*, 2015; Schuurman and Kleinhans, 2015; Williams *et al.*, 2016) and an increasing demand for understanding, predicting and controlling large braided rivers, we studied the morphological response of a braiding reach in the Yellow River to changing discharge regime.

Discharge regime is one of the determining factors in the evolution of large braiding rivers and rivers in general (e.g. Leopold and Wolman, 1957). It also has a large influence on channel dimensions, which is illustrated by an abundance of discharge-based hydraulic geometry relations (e.g. Leopold and Maddock, 1953; Parker *et al.*, 2007; Latrubesse, 2008), and on channel patterns (e.g. Leopold and Wolman, 1957; Kleinhans and Van den Berg, 2011). Furthermore, discharge variation affects the braiding river morphology and morphodynamics: a larger discharge variation increases the braiding intensity (Richard and Julien, 2003; Egozi and Ashmore, 2009; Nones *et al.*, 2013). Thus any significant change in high discharge conditions, either natural or human induced, is likely to affect the morphodynamics and eventually the larger-scale channel pattern in braiding rivers.

Morphodynamics in braiding rivers are an interplay between (mid-channel) bars, islands, channel branches and the floodplains (Bridge, 2003; Schuurman and Kleinhans, 2015). Together, these components form a commonly complicated braiding planform of which the dynamics are not well understood and difficult to predict. Nevertheless, several studies revealed characteristic behaviours in braiding rivers. For example, the balance of partitioning of flow and sediment at bifurcations was found to determine the evolution of individual mid-channel bars and islands, and through cumulative effects and propagation thereof, eventually decisive for the entire planform (Bridge, 2003; Nicholas, 2013a; Schuurman and Kleinhans, 2015). Another example is that formation of new channel branches in braiding rivers was found to occur by cross-bar flow after a (local) set-up of the water level due to the backwater effect of downstream non-uniformities (e.g. Schuurman and Kleinhans, 2015).

During higher discharges with overbank flow, the channel branches in braided rivers interact with the floodplains, among others through bank erosion and floodplain formation by aggradation and vegetation growth on floodplain-attached bars (Crosato and Saleh, 2010; Vesipa *et al.*, 2015; Schuurman *et al.*, 2016a; Lewin *et al.*, 2016). The balance between bank erosion and floodplain accretion determines the channel width–depth ratio and consequently the braiding intensity (e.g. Engelund and Skovgaard, 1973; Fredsoe, 1978; Struiksmas *et al.*, 1985; Ashworth *et al.*, 2000; Crosato and Mosselman,

2009; Rice *et al.*, 2009). Qualitatively, it is clear that bank erosion and floodplain accretion are of primary importance for the braiding pattern and morphodynamics. At the same time, these processes at the interface between channels and floodplains are among the most difficult processes to predict and to control in large braiding rivers, which has immediate societal relevance; for example, losses of fertile floodplains along large braiding rivers such as the Brahmaputra are hundreds of metres per year (Klaassen and 1992; Thorne *et al.*, 1993; Ahktar *et al.*, 2011; Baki and Gan, 2012).

Recent studies demonstrated the value of numerical models for expanding our fundamental understanding of the complicated morphodynamics in braiding rivers (Nicholas, 2013b; Yang *et al.*, 2015; Schuurman and Kleinhans, 2015; Sun *et al.*, 2015; Williams *et al.*, 2016). Among others, the numerical modelling of Nicholas (2013b) showed how bed properties such as grain size and morphodynamic processes such as riparian vegetation growth determine the channel dynamics and dynamic equilibrium channel pattern in large braiding rivers. The numerical models were able to capture general characteristics of river morphodynamics, including channel migration and bar dynamics (Schuurman and Kleinhans, 2015), and transitions between meandering and braiding river patterns (Nicholas, 2013a; Schuurman *et al.*, 2016b).

Numerical models can be considered complementary to field observations, flume studies and linear analyses, and are in particular convenient for comparing scenarios (Kleinhans *et al.*, 2010). With numerical models, the effects of disturbances in the river and changes in boundary conditions can be isolated from background morphodynamics (e.g. Schuurman and Kleinhans, 2015), in a controlled environment without the scaling issues of flume tests and without the many simplifications of analytical models.

Another advantage of numerical models is that they consider the gradual evolution of the river morphology, instead of being limited to end-members as in classical channel predictors and hydraulic geometry relations. For these reasons, the application of numerical models for predicting morphological effects of engineering works is common practice in relatively simple rivers, for example the single-thread river Rhine in the Netherlands, which has stabilized banks.

On the other hand, application of numerical models for river management in the more complicated large braiding rivers is still uncommon, although numerical modelling has a large potential for contributing to the understanding necessary for creating more diverse and reliable management schemes for large braiding rivers, ranging from optimizing river training works to river restoration. Thus numerical modelling can potentially contribute to mediating between social, ecological and economic values and uses of large braiding rivers.

Modelling of bar, island and floodplain destruction, which are indispensable processes in dynamic (equilibrium) rivers, is, however, still challenging (e.g. Williams *et al.*, 2016). Whereas the process of bar formation occurs on such a large scale that it is captured on coarse grids, the processes of bar, island and floodplain destruction require a fine grid to resolve steep erosive banks and small cross-cutting channels. Besides a high grid resolution with associated computational costs, the destruction of bars, islands and floodplains involves additional processes, such as undermining and failure of cohesive banks, that require identification of the bank line position in the model. This identification is a challenge, in particular in the case of modelling braiding rivers (Stecca *et al.*, 2017). When the necessary processes are not resolved, the planform pattern of growing bars leads to topographic forcing of bars as they develop towards equilibrium dimensions. As a result, the modelled river effectively becomes static after some time

(Schuurman *et al.*, 2013). While the static situation is often observed in single-thread rivers with fixed banks and, correctly, in models thereof, most braided rivers remain dynamic through the processes of chute channels and bar and floodplain destruction (Wheaton *et al.*, 2013), even in engineering contexts.

Research question and approach

The main research question of this study is: How do the channel planform and channel dynamics in a braiding reach of the Yellow River respond to an increase in annual peak discharge? Underlying research questions are: (1) What are the dominant morphodynamic processes following an increase in peak discharges? (2) What aspects of numerical model predictions are relevant to assess the effects of changing discharge conditions? (3) What processes need to be represented to prevent the modelled channel planform reaching an unrealistically static situation?

We simulated the hydro-morphodynamics of a Yellow River reach with several discharge conditions to answer the research questions. There is a continuum of model scenario detail, ranging from detailed model simulations with plenty of available data for construction, calibration and validation of the model (Williams *et al.*, 2013), to more conceptualized modelling in cases of data scarcity or an imaginary river case (Schuurman *et al.*, 2013; Nicholas, 2013b; Yang *et al.*, 2015). Arguably, an abundance of data does not necessarily result in better modelling or higher level of insight gained from the modelling. One reason is that model calibration often suffers from underdetermination, with different model settings giving the same result. Even with high-quality data, perfect reproduction of observations is not feasible (Kleinhans *et al.*, 2010; Williams *et al.*, 2013, 2016).

In this study we adopted an idealized modelling approach following Schuurman *et al.* (2013), Nicholas (2013b) and Yang *et al.* (2015), with simplified initial topography and development of a more complicated bar and channel topography by the numerical model. The modelling work can be distinguished in two parts: a calibration and sensitivity analysis based on the period 1999–2015, and modelling of different future discharge scenarios for the period 2015–2040. The future scenarios were used to formulate conclusions about the impact of higher peak discharges in the braiding reach of the Yellow River.

Study site

The study site is a 36 km reach of the Upper Yellow River. It is located in the Inner Mongolia region (Figure 1); it starts 40 km downstream of the city of Wuhai and ends at the city of Dengkou. This part of the Upper Yellow River is unconfined, and bordered by the Wulanbuh sand desert along the west bank and by a loess area along the east bank. The climate is arid, with annual precipitation of about 150mm and 60–70% of the precipitation occurring in the period July–September (Du *et al.*, 2014). The discharge in the Upper Yellow River varies between low discharges of about $500 \text{ m}^3 \text{ s}^{-1}$ in the winter and spring, to peak discharges of about $2000 \text{ m}^3 \text{ s}^{-1}$ in the summer (Figure 2a, b). The mean discharge is about $1000 \text{ m}^3 \text{ s}^{-1}$.

Based on field observations and satellite data, the study reach is classified as Laterally Active Braided following the classification scheme of Nanson and Knighton (1996). The average number of parallel channels (Braiding Index or BI) is

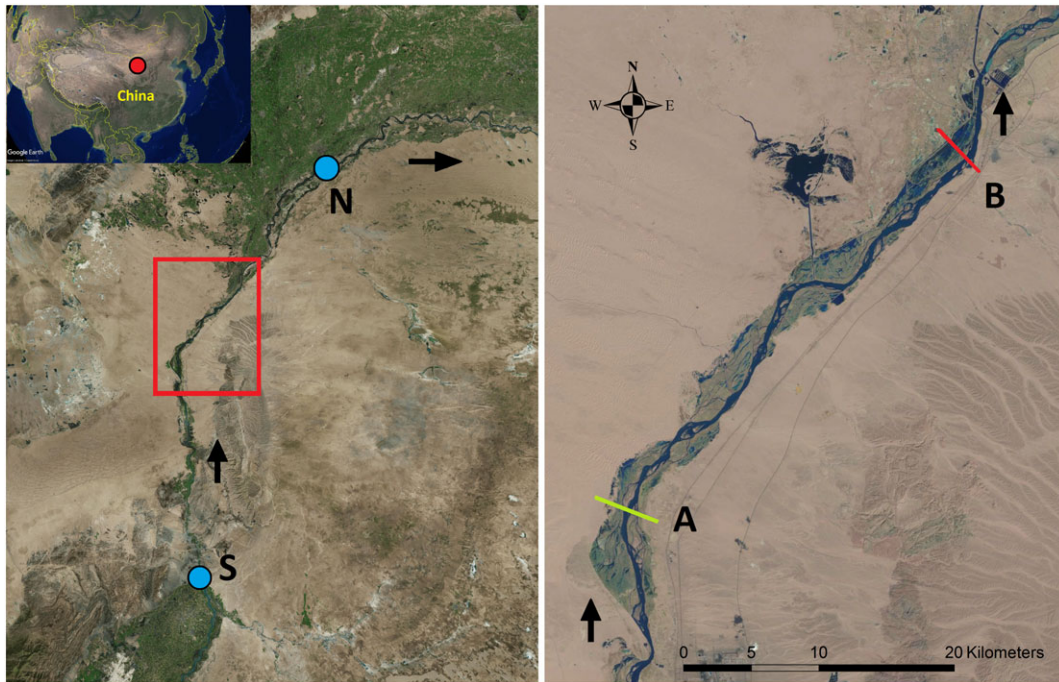


Figure 1. Location of the study reach in Inner Mongolia in the north of China. The study reach is located upstream of the city of Bayan Nur (location N), with the upstream boundary at line A and the downstream boundary at line B. The flow is from bottom left to top right. A discharge measurement station is located at the city of Shizuishan (S). Sources: top left Landsat / Copernicus, www.earth.google.com; left) Esri, DigitalGlobe, GeoEye, i-cubed, USDA FSA, USGS, AEX, Getmapping, Aerogrid, IGN, IGP, swisstopo, and the GIS User Community; right) Landsat 8, <https://earthexplorer.usgs.gov/>. [Colour figure can be viewed at wileyonlinelibrary.com]

about 1.5–2.0, computed using cross-sectional profiles and the average cross-section bed level as threshold to identify the channel branches (Figure 2c), with mid-channel bars present in the wider parts of the study reach. Most of the floodplain is an agricultural area and inundates during high discharge conditions. Aerial photographs of the study reach show evidence of former channel branches and sedimentation patterns on the floodplains.

Over the past decades, the study reach has experienced significant changes in the channel morphology: the channel width about halved, the BI decreased, and major aggradation occurred in the main channel (Figure 2c, d). These changes occurred simultaneously with a decline in river discharge (Figure 2a, b), attributed to a decline in precipitation, increase in water demand for irrigation and domestic use (Wang *et al.*, 2007; Xu *et al.*, 2009), and construction of hydropower dams with reservoirs (Ta *et al.*, 2008; Ma *et al.*, 2012). The largest reservoirs were formed after construction of the Liujiaxia dam in 1968 and the Longyangxia dam in 1986. The Liujiaxia dam is located about 800 km upstream of the study site, and the Longyangxia dam is located about 1200 km upstream of the study site.

Because the discharge of the Yellow River is insufficient to meet the water demands in the densely populated Lower Yellow River area, a South–North Water Transfer Project has been considered to connect the Yangtze River, which has an average discharge of about $30\,000\text{ m}^3\text{ s}^{-1}$, and the Yellow River (South-to-North Water Diversion Project Construction Committee, 2016; Webber *et al.*, 2017). In high Yangtze River discharge periods, part of the discharge will be transferred to the Yellow River and released from the hydropower reservoirs in the Yellow River. Two connections downstream of the study reach have already been made, and a third connection upstream of the study reach, the Western Route, is under consideration.

The discharge released from the hydropower reservoirs is expected to be altered after construction of the Western Route.

As a result, the discharge regime in a large part of the Yellow River will change, among others in the study site. It is expected that the peak discharges in the Yellow River will be increased, while the low discharges will not be changed. The new peak discharges are still uncertain, but are expected to be in the range of $2000\text{--}5000\text{ m}^3\text{ s}^{-1}$ and this peak discharge would continue for about 1 month per year (W. Ta, pers. comm.). The base discharge is likely to remain $500\text{ m}^3\text{ s}^{-1}$. The underlying goal of this study was to predict the potential morphodynamic impact of the increased peak discharge.

Model Description

General

We used the physics-based hydro-morphodynamic model Delft3D version 4.01.00. Delft3D solves the two-dimensional depth-average flow equations, with parametrization of the spiral flow, or the three-dimensional flow equations. The Delft3D model was used because of its common use in morphodynamic studies, its wide application in both science and engineering and its relatively high reliability (e.g. Lesser *et al.*, 2004; Schuurman *et al.*, 2013; Schuurman and Kleinhans, 2015; Williams *et al.*, 2016).

Hydrodynamics

In Delft3D, the hydrodynamics are modelled by applying depth-averaged momentum (Eqs. (1) and (2)) and continuity (Eq. (3)):

$$\frac{\partial u}{\partial t} + u \frac{\partial u}{\partial x} + v \frac{\partial u}{\partial y} + g \frac{\partial z}{\partial x} + \frac{g v \sqrt{u^2 + v^2}}{C^2 h} + v \frac{\partial^2 u}{\partial x \partial y} + F_x = 0 \quad (1)$$

$$\frac{\partial v}{\partial t} + u \frac{\partial v}{\partial x} + v \frac{\partial v}{\partial y} + g \frac{\partial z}{\partial y} + \frac{g u \sqrt{u^2 + v^2}}{C^2 h} + v \frac{\partial^2 v}{\partial x \partial y} + F_y = 0 \quad (2)$$

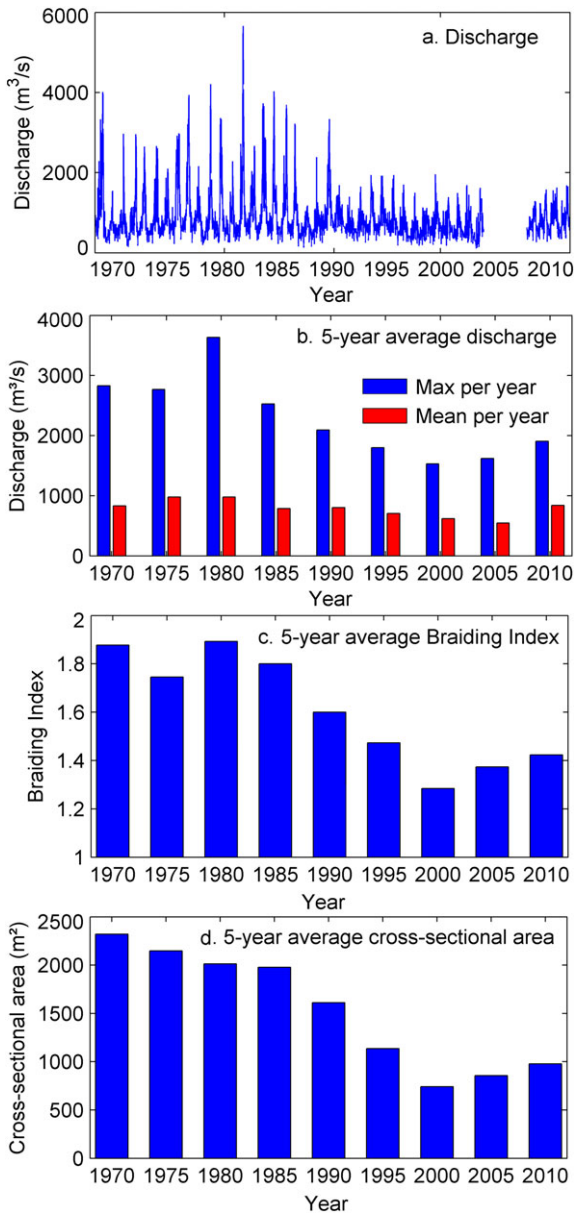


Figure 2. (a) Measured discharge at Shizuishan (location S in Figure 1); (b) 5-year average maximum and mean annual discharge at Shizuishan; (c) 5-year average BI; (d) 5-year average cross-sectional area. [Colour figure can be viewed at wileyonlinelibrary.com]

$$\frac{\partial h}{\partial t} + \frac{\partial hu}{\partial x} + \frac{\partial hv}{\partial y} = 0 \tag{3}$$

where x is the downstream coordinate (m), y is the lateral coordinate (m), z is the bed level (m), u is flow velocity in the x -direction ($m s^{-1}$), v is flow velocity in the y -direction ($m s^{-1}$), h is the water depth (m), C is the Chézy roughness ($m^{0.5} s^{-1}$), g is the gravity acceleration constant ($m s^{-2}$), ν is the horizontal eddy viscosity ($m^2 s^{-1}$) and $F_{x,y}$ is the acceleration term due to streamline curvature ($m s^{-2}$).

In order to test the parametrization of the spiral flow in the two-dimensional model, we conducted two simulations with three-dimensional hydrodynamics. For three-dimensional hydrodynamics, an extra term for the vertical flow is added to Eqs. (1) and (2), and Eq. (3) is adjusted to include the vertical flow. In one of the three-dimensional simulations, the vertical was divided into three layers, with the lowest layer containing 10% of the water depth, the middle layer containing 30% and the upper layer containing 60%. In the other three-dimensional simulation, the vertical was equally divided

into seven layers. For further details concerning the numerics and physics of the three-dimensional flow, see, for example, Lesser *et al.* (2004), Schuurman *et al.* (2013), Schuurman and Kleinhans (2015) and Williams *et al.* (2016).

Delft3D computes the hydrodynamics by applying a finite difference method and the hydrostatic pressure assumption. The Alternating Direction Implicit method is used to solve the differential equations, by splitting each time step into two parts: the first half to solve in the x -direction and the second half to solve in the y -direction. In two-dimensional simulations, the vertical flow is parametrized in order to include the effect of streamline curvature-induced spiral flow. Turbulence closure is achieved by applying a constant uniform horizontal eddy viscosity. For a detailed description of the flow computation and numerical scheme, see Lesser *et al.* (2004), Van der Wegen and Roelvink (2008) and Deltares (2009).

Sediment transport and morphodynamics

The morphodynamic computation in Delft3D includes capacity-limited sediment transport induced by the flow, sediment deflection by bed slope, bank erosion and update of the bed level. We applied the bed material load predictor of Engelund and Hansen (1967):

$$q_s = \frac{0.05 U^5}{\sqrt{g} C^3 \Delta^2 D_{50}} \tag{4}$$

where q_s is the total sediment transport per unit width ($m^2 s^{-1}$), U is the depth-averaged flow velocity in streamline direction ($m s^{-1}$), Δ is the relative mass density of submerged sediment (–) and D_{50} is the median grain size (m).

At the upstream boundary, the amount of sediment entering the system was set to be in equilibrium with the local sediment transport capacity. This procedure prevented erosion or deposition at the upstream boundary. It implied that the sediment input was higher in high discharge periods, when also the sediment transport capacity was relatively high. Although the sediment released by the upstream hydropower dams and the local sediment transport capacity directly downstream of the dams might not be in equilibrium all the time, it is assumed that the sediment transport at the upstream boundary of the study reach reached an equilibrium due to the large distance from the upstream dams (about 800 km to the Liujixia dam). Sediment sources to regain equilibrium are, among others, channel bed incision and bank erosion.

The sediment transport direction is deflected from the depth-averaged flow velocity by spiral flow in a channel bend and by gravity on a bed slope (Talmon *et al.*, 1995). The spiral flow deflects the sediment transport direction towards inner bends, which can be a point bar in the case of a meandering channel, or a mid-channel bar or bank-attached bar in the case of a braided channel. In two-dimensional simulations in Delft3D, the angle ϕ_τ between the sediment transport vector and the downstream direction (x -axis) is computed by

$$\tan(\phi_\tau) = \frac{v}{u} - A \frac{h}{R} \tag{5}$$

where R is the radius of the local streamline curvature (m) and, assuming a logarithmic flow velocity profile, the spiral flow coefficient A is computed by

$$A = E_s \frac{2}{\kappa^2} \left(1 - \frac{\sqrt{g}}{\kappa C} \right) \tag{6}$$

where κ is the Von Kármán constant (0.4) and E_s is a calibration parameter. Next, the sediment transport direction is corrected for the bed slope effect by

$$q_x = q_s \left(\cos(\phi_\tau) - f(\theta) \frac{\partial z_b}{\partial x} \right) \quad (7)$$

$$q_y = q_s \left(\sin(\phi_\tau) - f(\theta) \frac{\partial z_b}{\partial y} \right) \quad (8)$$

where

$$f(\theta) = \frac{1}{\alpha\theta\beta} \quad (9)$$

in which θ is the Shields mobility parameter and α and β are calibration parameters. A larger α means a smaller bed slope effect and thus a smaller effect of gravity on the grains. The parameter β is kept at a constant value of 0.5, in agreement with, for example, Ikeda and Nishimura (1986), Talmon *et al.* (1995) and Parker *et al.* (2003).

The bed level is updated in each time step based on the sediment transport rate and direction, using the Exner equation to meet mass conservation:

$$\frac{\Delta z_b}{\Delta t} = \frac{f_m}{(1-p)} \left(\frac{\Delta q_x}{\Delta x} + \frac{\Delta q_y}{\Delta y} \right) \quad (10)$$

where p is the porosity (0.4) and a morphological acceleration factor f_m is applied at each time step to accelerate the computation. This factor can be applied because the adaptation time for morphology is much larger than for water flow and because a change in flow field is only caused by a change in the morphology, while such change within a hydrodynamic time step is extremely small. The morphological acceleration factor can also be regarded as a bridge between short-term hydrodynamics and long-term morphodynamics (Roelvink, 2006). The effect of the factor on bed morphology is usually negligible (Roelvink, 2006; Crosato *et al.*, 2011), but large flow velocity gradients require a relatively small factor to prevent numerical instability and inaccuracy (Williams *et al.*, 2016).

For sediment transport, a threshold water depth of 0.1 m was applied. Grid cells with smaller water depth were considered to be inactive. Inactive grid cells were reactivated when the water depth became larger than the threshold depth. Additionally, dry cells were reactivated by a simple bank erosion algorithm; erosion of a dry grid cell occurred when erosion took place in a neighbouring wet grid cell. The amount of erosion in the neighbouring wet cell was fully transferred to dry grid cell to stimulate bank erosion and lateral channel shift.

Model grid and initial bed level

Figure 3 shows the computational domain and initial bed level, and the general grid properties are given in Table I. The computational grid included floodplain area to enable lateral shift of the main channel. The grid was designed in such way that the main channel in 1999 consisted of at least 12 grid cells in a transverse direction. Commonly, the main channel consisted of many more grid cells (Figure 3b). The outer lateral borders of the grid domain were defined by dykes along the floodplains, identified from satellite images by the inundation extent during periods of high water levels. The grid cell sizes varied from 40 to 60 m in the longitudinal direction and from 22 to 30 m in the transverse direction, making the aspect ratio about 1.5 to 2.4. In total, 703 grid cells in the longitudinal direction and 162 grid cells in the transverse direction were used.

Table I. Initial conditions and default input parameters for the model runs

| Parameter | Unit | Value |
|------------------------------|------------------|-----------------------|
| Channel length | m | 36 000 |
| Initial bed slope | — | 2.3×10^{-4} |
| C (Eqs. (1) and (2))* | $m^{0.5} s^{-1}$ | 45 |
| D_{50} (Eq. (4))* | m | 1.10×10^{-4} |
| E_s (Eq. (6))* | — | 2.0 |
| α (Eq. (9))* | — | 0.20 |
| β (Eq. (9)) | — | 0.5 |
| f_m (Eq. (10)) | — | 4 or 25 |
| Sediment transport predictor | — | EH |
| Grid cell length | m | 40–60 |
| Grid cell width | m | 22–30 |
| Hydrodynamic time step | s | 30 |
| Morphodynamic time step | s | 120 or 750 |

* Denotes that a sensitivity analysis is conducted for input parameters.

The initial bed levels used in this study were based on a combination of information from satellite images and measured bed-level cross-sections to schematize the larger-scale morphological units. First, based on the satellite images, the model domain was classified in three groups of large-scale morphological units: channel, bare dry area (bars) and dry vegetated area (floodplain and islands). Secondly, each group was given a characteristic relative surface level, based on the measured cross-sections: the surface level of the bars was about 2 m higher than the channel bed, and the vegetated areas were about 4 m higher than the channel bed. Thirdly, a uniform longitudinal valley slope of 23 cm km^{-1} was applied, following Yao *et al.* (2011). For constructing the bathymetry of 1999 we applied a LandSat 7 image with a date of 12 August 1999, and for the 2015 bathymetry we applied a LandSat 8 image with a date of 25 March 2015. The smaller-scale units such as low bars and channel branches were formed by the morphological model during the simulation. An initial uniform bed layer thickness of 10 m was applied.

In the post-processing and for making 2D maps of the modelled bed level, we corrected for the initial valley slope. The averaged bed level in each cross-section was used as a threshold to identify the channel branches in the braidplain, from which the BI was derived. For the future scenarios, we calculated the braidplain width by taking the distance between the two outermost channel branches in each cross-section. In addition, we calculated an alternative braidplain width by considering sedimentation on the floodplains, taking the distance between the two outermost locations of floodplain sedimentation in excess of an arbitrary 0.5 m, which is 12.5% of the initial channel depth.

Boundary conditions

Two different periods were modelled: 1999–2015 for calibration and sensitivity analysis of several input parameters, and 2015–2040 for future scenarios using the best-fitting input parameters. For the period of 1999–2015, a hydrograph was constructed with four continuous months of high discharge ($1100 \text{ m}^3 \text{ s}^{-1}$) and eight continuous months of low discharge ($500 \text{ m}^3 \text{ s}^{-1}$); see the schematized hydrograph in Figure 4a. The future scenarios were simulated with a hydrograph of 1 month of peak discharge and 11 months of low discharge (Figure 4b). The low discharge was again $500 \text{ m}^3 \text{ s}^{-1}$, and the peak discharge varied between 2000 and $4000 \text{ m}^3 \text{ s}^{-1}$.

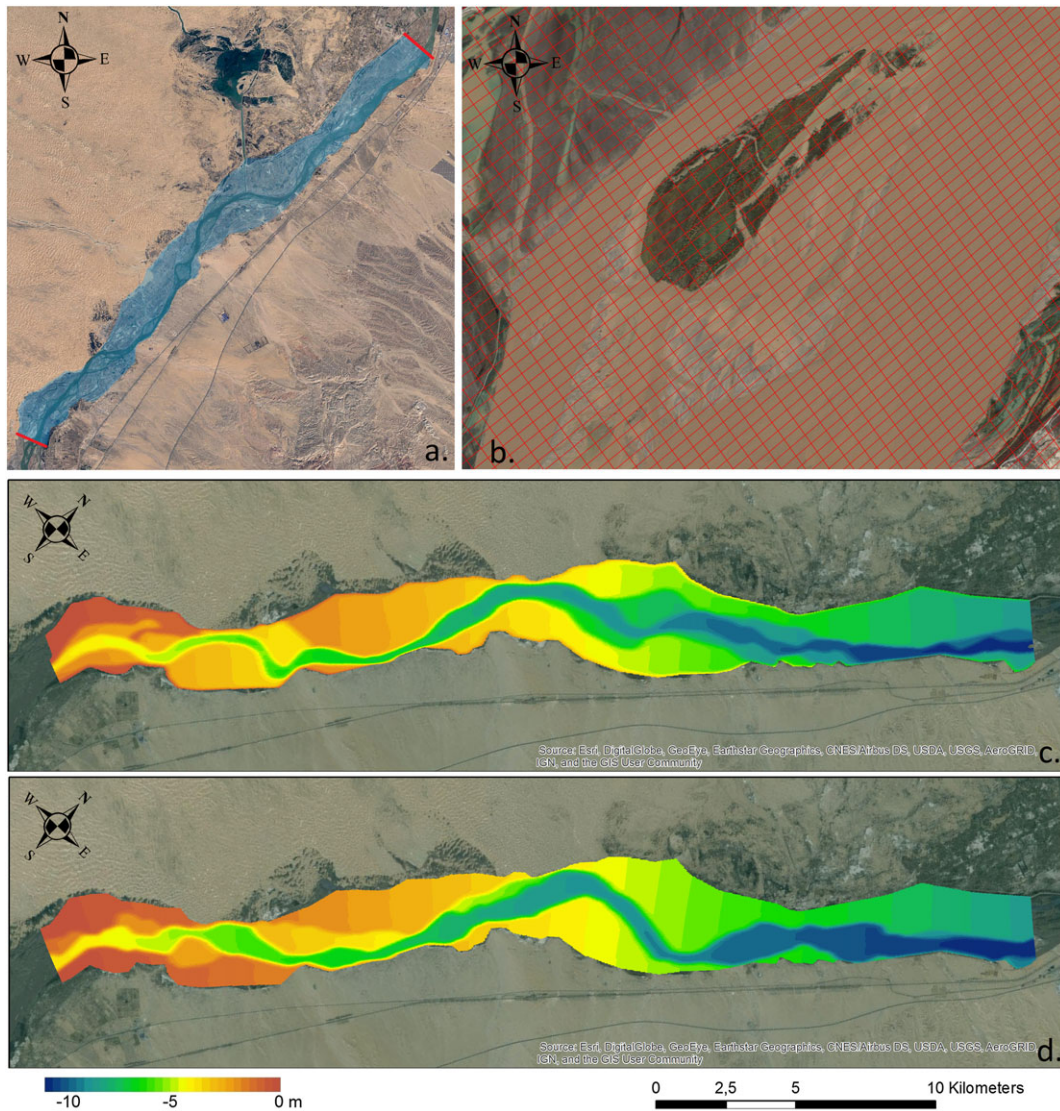


Figure 3. (a) Computational grid with hydrodynamic boundaries, with flow from southwest to northeast. (b) Detail of the grid. (c) Initial bed level of 1999, with flow from left to right. (d) Initial bed level of 2015. Sources: a) Landsat / Copernicus, www.earth.google.com; b) DigitalGlobe 2012, www.earth.google.com; c, d) Esri, DigitalGlobe, GeoEye, Earthstar Geographics, CNES/Airbus DS, USDA, USGS, AeroGRID, IGN, IGP, swisstopo, and the GIS User Community. [Colour figure can be viewed at wileyonlinelibrary.com]

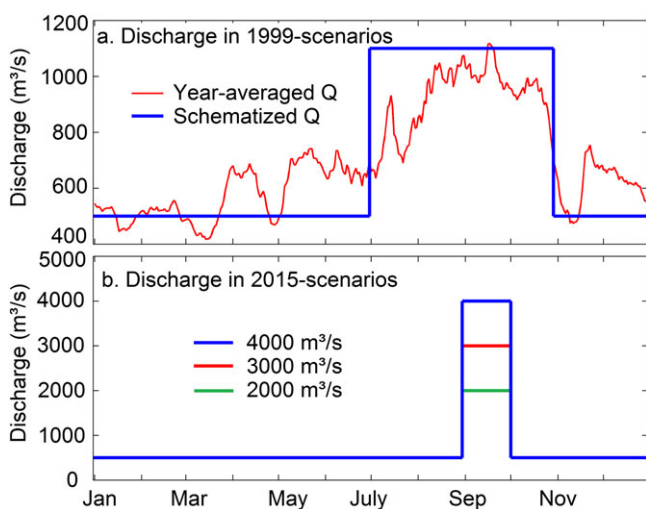


Figure 4. (a) Average measured discharge for the period after 1986 and the schematized hydrograph for modelling of the 1999 scenarios. (b) Hydrograph for modelling of the future scenarios with peak discharges of 2000, 3000 and 4000 $\text{m}^3 \text{s}^{-1}$. [Colour figure can be viewed at wileyonlinelibrary.com]

These discharge conditions were based on the expected future discharge regime (W. Ta, pers. comm.).

At the downstream boundary, a $Q-h$ water level relation was imposed. As water level measurement data were not available for the study reach, the Chézy formula was used to estimate the water depth and water level for each discharge.

A spin-up period was applied between each change in upstream discharge and downstream water level. In this period, the discharge gradually changed to the new discharge, and the hydrodynamics could adapt to the new discharge and water level. Bed level change was disabled in the spin-up period.

Other model settings

An overview of the other model settings is given in Table I. One of these settings is the bed roughness parametrization. In the calibration runs from 1999, we compared different bed roughness parametrizations: a constant, uniform Chézy roughness and two constant, uniform Nikuradse k_s roughness values. Delft3D uses the Chézy roughness C as input for the momentum equations (Eqs. (1) and (2)) and sediment transport

formula (Eqs. (4) and (6)). In Delft3D, Nikuradse k_s is converted into Chézy roughness C by

$$C = 18 \log \left(\frac{12h}{k_s} \right) \quad (11)$$

A constant and uniform k_s of 0.15 m was used as default for the calibration runs from 1999. We also applied a k_s of 0.30 m and a C of $45 \text{ m}^{0.5} \text{ s}^{-1}$. For all future scenarios from 2015, we applied a constant and uniform C of $45 \text{ m}^{0.5} \text{ s}^{-1}$, because this bed roughness parametrization gave the best results in the calibration.

The reason for comparing the different bed roughness parametrizations is to determine the effect of spatial and temporal bed roughness variations, which are known to have a minor effect on bar height and pool depth (Schuurman *et al.*, 2013). Applying a uniform and constant Chézy roughness C means that the ratio between the water depth and Nikuradse roughness length is assumed constant, meaning smaller roughness in shallower water. Alternatively, applying a uniform and constant Nikuradse k_s means that the spatially variable water depth is used in the conversion to C (Eq. (11)).

Vegetation dynamics that affect the flow and sediment transport are, however, not considered, despite recent progress in the modelling of vegetation dynamics (Bertoldi *et al.*, 2014; van Oorschot *et al.*, 2016). One reason for not modelling vegetation dynamics is the relatively uniform coverage of agricultural crops on the floodplains, based on satellite images, which would reduce the impact of dynamic vegetation modelling. Also, the presence of minor dykes and roads in the floodplains are not accounted for, which is expected to have a larger effect than the vegetation and will be discussed later.

For the bed slope parameter α , a default value of 0.2 was used. In the literature, a range of values of the order of 1 has been proposed (e.g. Talmon *et al.*, 1995; Struiksmā *et al.*, 1985). Because of the range of values given in the literature and the sensitivity of the bed morphology to the parametrization (Schuurman *et al.*, 2013), the effect of the bed slope parameter on bed morphology was determined. For the spiral flow intensity, an E_s of 2.0 was applied by default, and its channel pattern was compared with the channel pattern in the cases of E_s of 1.0 and three-dimensional hydrodynamics.

A uniform median grain size of $110 \mu\text{m}$ was applied, following Lischan *et al.* (2010) and Ta *et al.* (2011). Although the river transports a large amount of finer material, this fine material is hardly deposited in the main channel (Ta *et al.*, 2003) and thus hardly affects the bar and branch dynamics. The downstream coarsening caused by lateral input of relatively coarse desert sand (Ta *et al.*, 2003; Wang *et al.*, 2015) was neglected. In order to determine the effects of coarser sediment on the channel pattern, we conducted two extra simulations with uniform median grain sizes of 160 and $220 \mu\text{m}$.

Due to the high fine sediment concentration, relatively high viscosity and sediment diffusivity parameters were used: 10 and $100 \text{ m}^2 \text{ s}^{-1}$. In general, high values for viscosity and diffusivity cause damping of small eddies, resulting in relatively large-scale sediment erosion and deposition features.

Time steps of 30 s were used to solve the hydrodynamics. For computation of the bed level change, different morphological acceleration factors f_m (Eq. (10)) were used. In the model runs that started in 1999, with a peak discharge of $1100 \text{ m}^3 \text{ s}^{-1}$, an f_m of 25 was applied for the low discharge period and an f_m of 4 for the high discharge period. In the future discharge scenarios, an f_m of 10 was applied for the low discharge period and an f_m of 4 for the peak discharge period. The lower factor for the peak discharge period and the lower factor for the future scenarios were required to prevent numerical instability.

Results for 1999–2015: Calibration and Sensitivity Analysis

In this section we present the results of the calibration and sensitivity analysis. The bed level of 1999 was used as initial situation, and the simulations were run until 2015. At the upstream boundary, we imposed the schematized hydrograph of Figure 4a. First, we describe the modelled channel evolution for the calibrated model settings. Next, we assess the sensitivity of the modelled channel evolution for bed roughness, bed slope effect, spiral flow parametrization and median grain size.

Bar and channel dynamics from 1999 using default settings

The development of bars and branches in the braiding reach of the Upper Yellow River is shown in Figure 5. The development started with the initiation of mid-channel and bank-attached bars within the initial channel. Different kinds of bar and channel patterns were formed for different parts of the modelled reach, mainly discriminated by the local channel width. In the upstream part (A in Figure 5), a relatively large number of small bars were formed within 1 km from the upstream boundary.

In the following years, these bars merged and formed a complex bar without a clear main channel. Another part of the modelled reach, the low-laying area at B, was inundated during high discharge and channels formed in it. In the narrow section at C, the width–depth ratio was probably too small for bar formation. Further downstream, where the channel was wider, a large bank-attached bar formed along the left bank and bank erosion occurred along the right bank. At location E, the low-laying areas were eroded and new branches formed on it. After about 10 years, a large bar was formed along the right bank by merging of multiple smaller bars.

The peak discharge of $1100 \text{ m}^3 \text{ s}^{-1}$ was insufficient to inundate the floodplains, leaving the floodplain surface untouched and only affecting the floodplains by bank erosion. At the same time, the initial bars were subjected to severe deposition and channel formation. The width–depth ratio of the main channel appeared decisive for the formation of mid-channel bars, as explained before by linear analyses and numerous examples from rivers and flume experiments. The channel width–depth ratio is determined by a balance between bank erosion and floodplain accretion. Therefore, reproduction of bank erosion and floodplain accretion is important for accurate modelling of the bar and channel dynamics. In the simulations started from 1999, the amount of bank erosion and lateral channel shift of the main channel appeared to be relatively small. This outcome is in contrast to the severe bank erosion and lateral channel shift as shown by aerial photographs of the study reach for the same period as the simulations. Possible reasons why the amount of bank erosion was underestimated are considered in the discussion section.

The next sections elaborate on the sensitivity of the bar and channel pattern, especially the BI, and the bar and channels dynamics to various input parameters and model settings. These results partly served the calibration of input parameters, and were partly used to determine the sensitivity of the channel pattern and dynamics to input parameters.

Sensitivity to bed roughness

The effect of bed roughness parametrization on the channel pattern in the braiding reach is shown in Figure 6a, and 2D

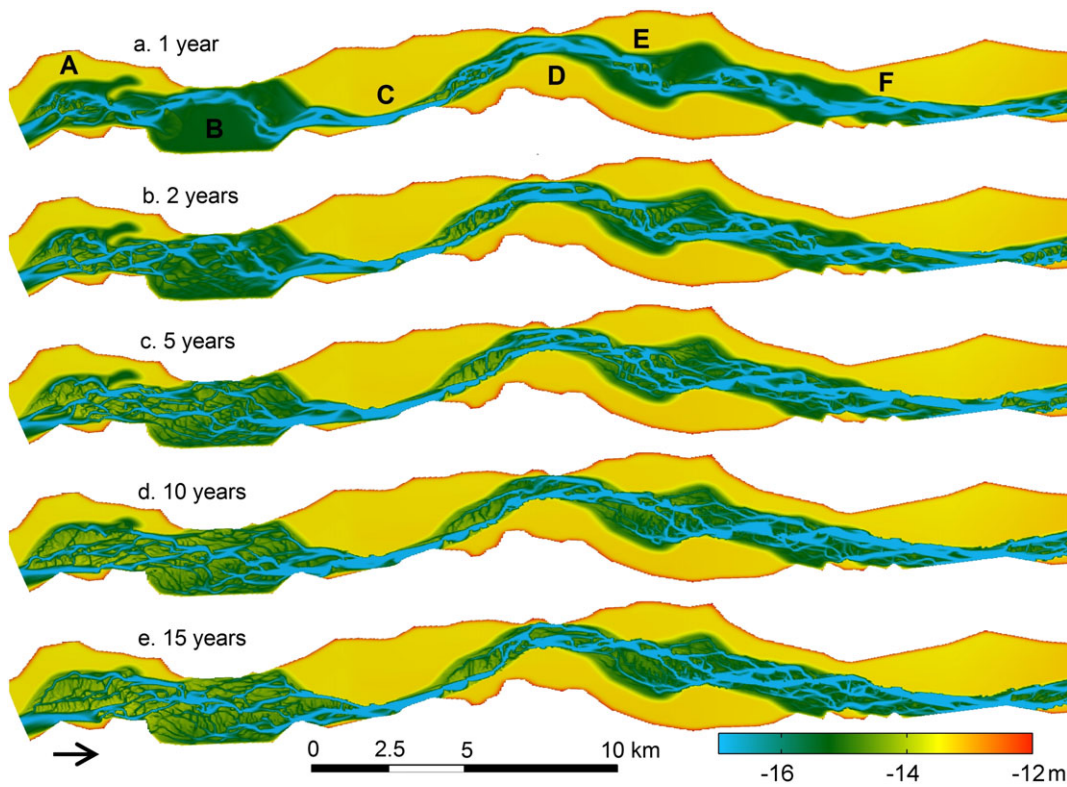


Figure 5. Time series of the modelled bed level for default settings and present discharge conditions starting from 1999. Flow is from left to right. [Colour figure can be viewed at wileyonlinelibrary.com]

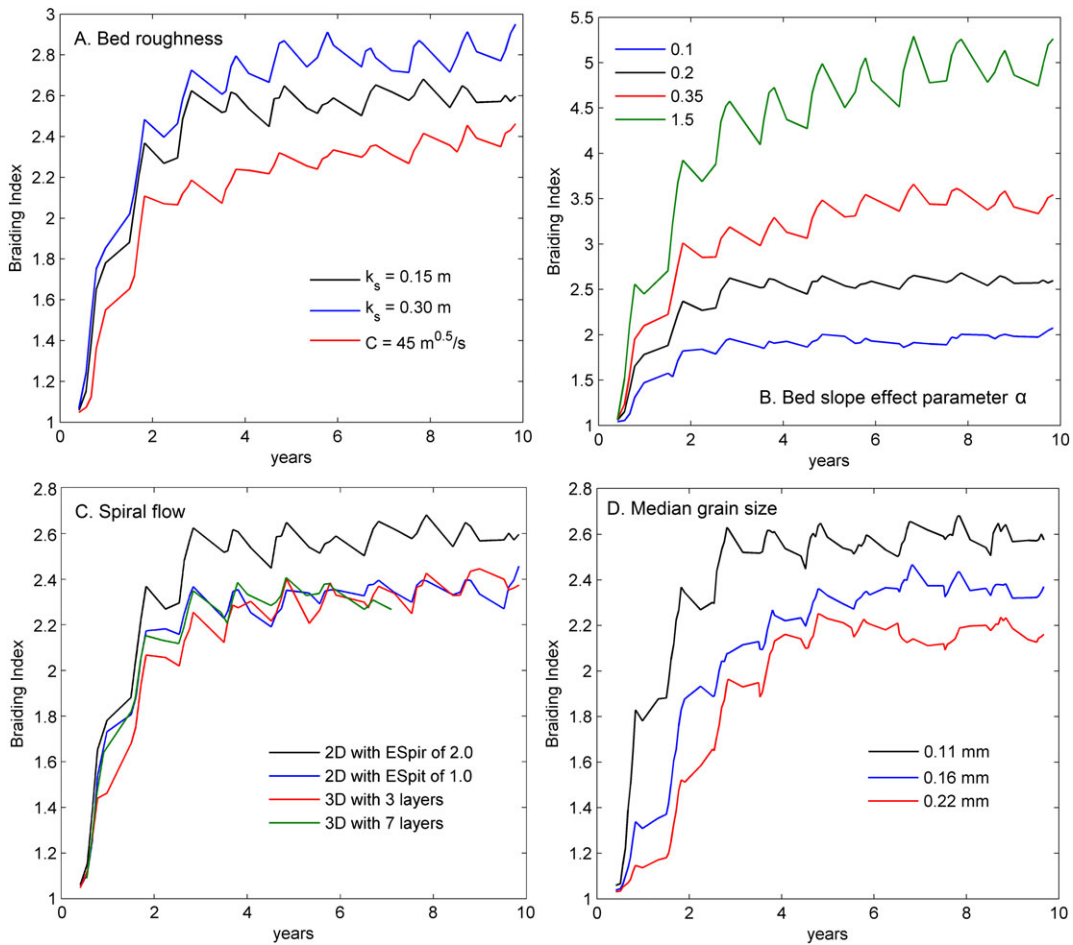


Figure 6. Time series of the reach-averaged BI for different settings for (A) bed roughness, (B) bed slope parameter α , (C) spiral flow parameter E_s or 3D flow, and (D) median grain size. [Colour figure can be viewed at wileyonlinelibrary.com]

figures are available in the supplementary material as supporting information. The difference in bar pattern between k_s of 0.15 m and 0.30 m was relatively small: the dimensions and number of bars were about the same. In contrast, the difference between a constant Chézy bed roughness C and constant k_s values was relatively large: a constant C resulted in fewer and larger mid-channel bars. Furthermore, the bed was smoother with lower bars. The latter observation can be explained by the conversion of the k_s to C for the momentum equation, which resulted in a lower C on the bars (small h) and a larger C in the deeper channels (large h). The bar pattern formed with a constant C seemed to fit best with the field observations: a low BI, and small slope and smooth bar edges.

Sensitivity to bed slope effect

Figure 7 shows the braiding study reach after 14 years for different values of α (Eq. (9)). The value of α had a large effect on the bar pattern, with many small bars in the case of a large α and fewer, larger bars in the case of a small α . This result is supported by time series of the BI in the model simulations (Figure 6). The measured average BI in the study reach was about 1.5–2 (Figure 2), which is best obtained with an α of 0.1 or 0.2.

Also, the depth of the channels and bed level variation of the braidplain were affected by the bed slope effect parametrization: a large α resulted in relatively high bar surfaces, steep bar edges and deep branches (Figure 7). Thus the bed slope effect had a clear smoothing effect. Overall, an α of 0.1 slightly underestimated the bed level variation, whereas an α higher than 0.2 overestimated the bed level variation.

For the future discharge scenarios, we choose to apply an α of 0.2. This value was several times smaller than commonly

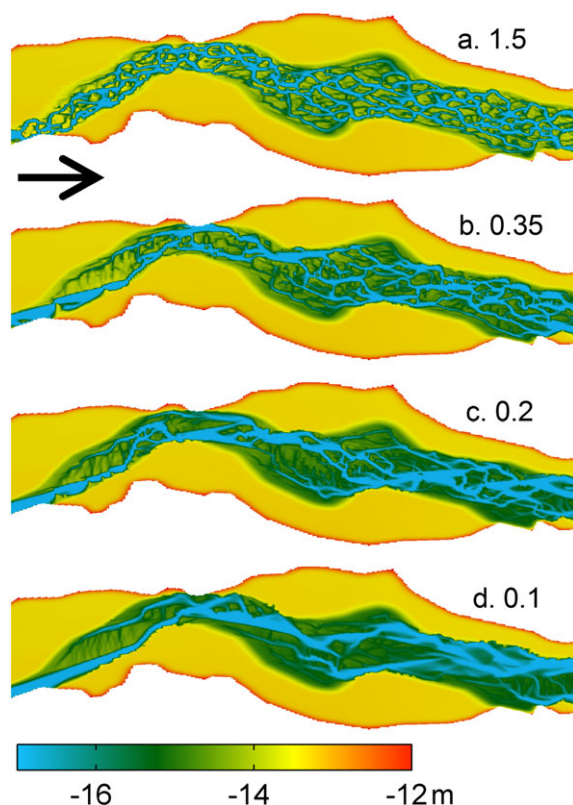


Figure 7. Sensitivity of morphology to the bed slope parameter α after 14 years, started in 1999. Flow is from left to right. [Colour figure can be viewed at wileyonlinelibrary.com]

applied values of α , such as 0.7 (Schuurman *et al.*, 2013; Schuurman and Kleinhaus, 2015) and 1.7 (Crosato and Mosselman, 2009). However, the α should be relatively small to compensate for the relatively high spiral flow intensity forced to stimulate bank erosion and lateral channel migration. Also, Koch and Flokstra (1981) indicated that α depends on the grain size, with larger D_{50} resulting in a larger α . In the current study, a relatively small D_{50} was applied, which might explain the relatively small α found most suitable for modelling of the braiding study reach in the Upper Yellow River.

Sensitivity to spiral flow parametrization

The bed slope effect is counteracted by the spiral flow in the case of streamline curvature. The results for different values of E_s and for the three-dimensional simulations are given in Figure 6c. First, the simulations with an E_s of 1.0 gave similar BI values to both three-dimensional flow simulations. This result could be interpreted as a demonstration of the reliability of the spiral flow parametrization in the two-dimensional simulations. Second, the E_s of 2.0 gave a higher BI of 2.6 than an E_s of 1.0 (BI of 2.4). Thirdly, the simulations confirm that the bed topography and channel pattern are much less sensitive to the parameter E_s than to the transverse bed slope effect parameter α . Although an E_s of 1.0 seemed to be the safe choice, we applied an E_s of 2.0 in the future scenarios in order to stimulate deepening of outer bends, and with that stimulating bank erosion and lateral channel shift.

Sensitivity to grain size

Figure 6d shows the result for different median grain sizes, including the default D_{50} of 0.11 mm. The equilibrium BI was about 23% lower for a doubled median grain size of 0.22 mm. For a median grain size of 0.16 mm, the BI was about 11% lower than the default median grain size of 0.11 mm. Thus a coarsening of the channel bed by a factor of two lowered the BI by a factor of about 0.25. Following the analytical model of Crosato and Mosselman (2009), a bed coarsening by a factor of two was expected to give a decline in BI of about 16%, and a coarsening by a factor of 1.5 should give a decline of about 10%. Thus the channel pattern in the simulations of the current study is slightly more sensitive to the median grain size than the analytical model. One explanation for this outcome is the occurrence of nonlinear and indirect effects, such as a change in width–depth ratio after a change in median grain size.

Results for Future Discharge Scenarios

In this section we show and describe the modelled channel evolution in the period 2015–2040, applying the future discharge scenarios with different annual peak discharges. First, the channel pattern and evolution for the different scenarios are given. Next, the model results for a non-uniform bed roughness parametrization are shown. After this, alternative future discharge scenarios are considered.

Channel pattern and evolution

The bed level simulated by the Delft3D model for a peak discharge of $3000 \text{ m}^3 \text{ s}^{-1}$ over the period 2015–2040 is given in Figure 8. Time series of the bed level for the other future scenarios are available as supporting information. Similar to

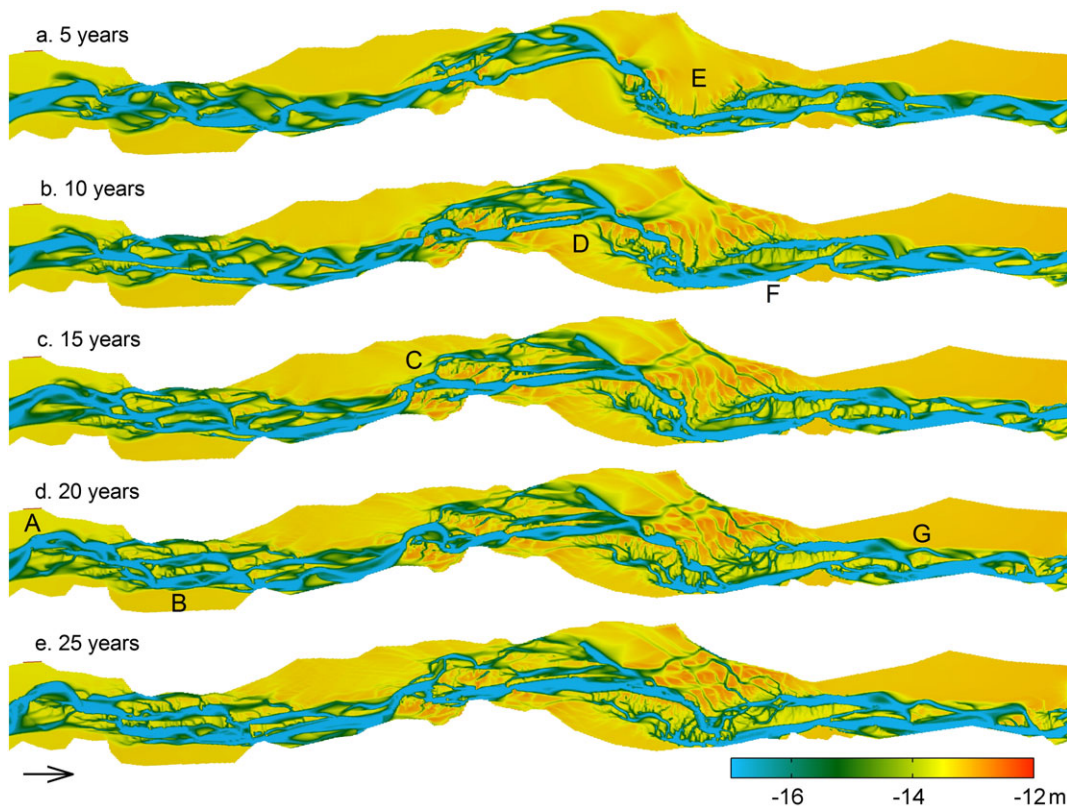


Figure 8. Time series of the modelled bed level for an annual peak discharge of $3000 \text{ m}^3 \text{ s}^{-1}$, starting in 2015. Flow is from left to right. [Colour figure can be viewed at wileyonlinelibrary.com]

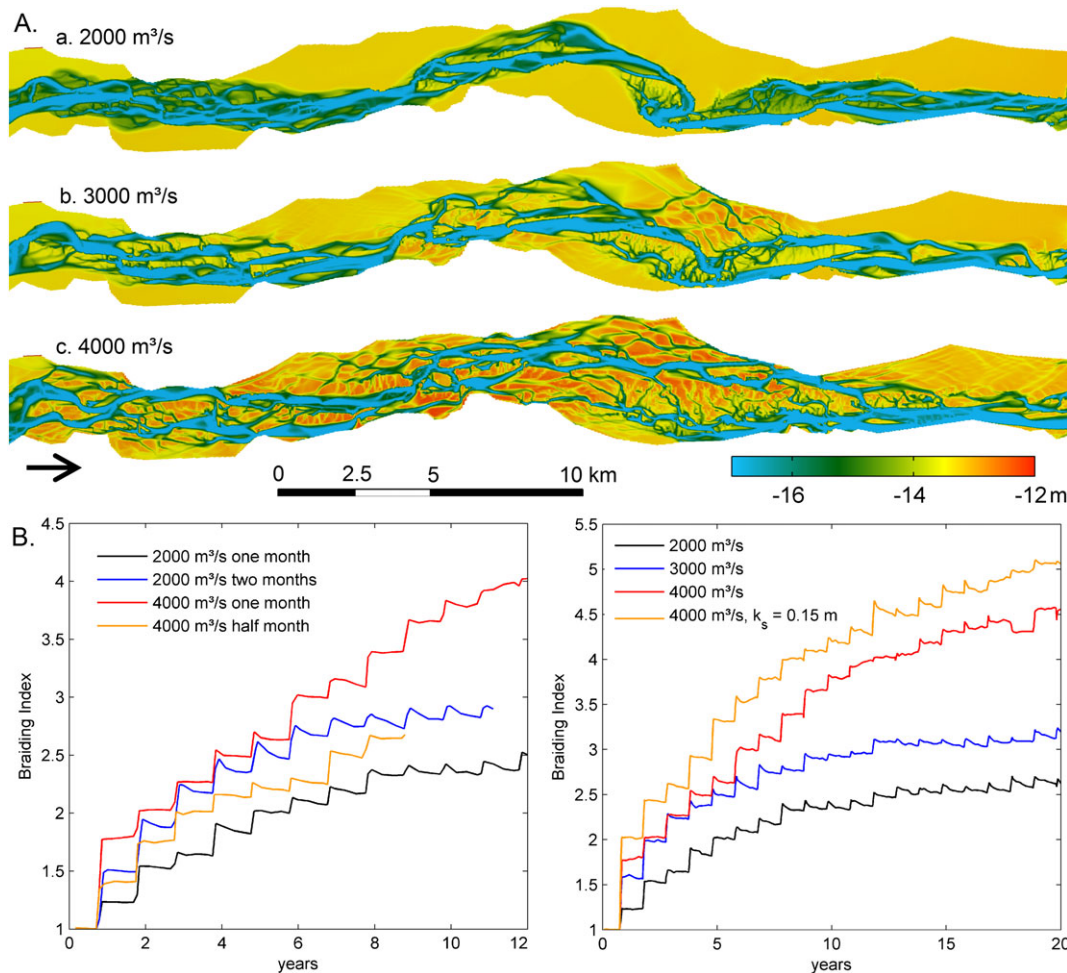


Figure 9. (A) Modelled bed level after 25 years for different peak discharges. (B) Times series of the reach-averaged BI for different discharge scenarios. See supporting information for sensitivity to roughness parametrization. [Colour figure can be viewed at wileyonlinelibrary.com]

the simulation of 1999 (Figure 5), mid-channel banks and bank-attached bars formed in the initial main channel. In the future scenarios, these bars were much larger than in the simulation of 1999, especially in the case of a peak discharge of 3000 or 4000 $\text{m}^3 \text{s}^{-1}$. In the future scenarios, bar lengths of several kilometres were common.

In later stages, the peak discharges in the future scenarios gave rise to interaction with the floodplains, with lateral channel shift by means of bank erosion and avulsions. For example, bank erosion of several hundreds of metres occurred along main channel (features A, B and C in Figure 8); and at features D and E of Figure 8 the flow over the floodplains formed major head-cutting channels on the floodplain. These channels expanded in an upstream direction. Lateral shift of channel branches also resulted from instability of bifurcations, for example at the large mid-channel bar of feature F in Figure 8 and at the bank-attached bar at G.

Figure 9 shows the modelled bed level in 2040 for the scenarios with peak discharges of 2000, 3000 and 4000 $\text{m}^3 \text{s}^{-1}$. A clear difference in channel evolution can be identified between the three peak discharge scenarios: in the simulation with 2000 $\text{m}^3 \text{s}^{-1}$ the channel evolution was limited to the bars and branches within the braidplain and minor bank erosion occurred. In the simulation with a peak discharge of 3000 $\text{m}^3 \text{s}^{-1}$ the channel evolution extended to the floodplains. Chute channels were formed on the floodplain and bank erosion caused widening of the main channel. In the simulation with peak discharge of 4000 $\text{m}^3 \text{s}^{-1}$ major changes in the main channel and on the floodplains occurred: the formation of many chute channels on the floodplains, widening of the main channel by bank erosion, major lateral shift of the channel branches, bar migration and bifurcation instability. Also, about 0.5–1.0 m of sediment was deposited on top of the floodplains during high discharge. This deposition was accompanied by formation of relatively small branches on the floodplains. Some of these branches evolved to a dominating branch, closing the original dominant branch.

The BI is given in Figure 9. It shows the effect of the peak discharge on the BI: a higher peak discharge resulted in a higher BI. After 20 years, the BI for a peak discharge of 2000 $\text{m}^3 \text{s}^{-1}$ was about 2.6, whereas a peak discharge of 3000 $\text{m}^3 \text{s}^{-1}$ resulted in a BI of about 3.5. A peak discharge of 4000 $\text{m}^3 \text{s}^{-1}$ resulted in a BI of about 4.5.

The width of the channel or braidplain was also strongly affected by the peak discharge (Figure 10). The reach-averaged braidplain width for a peak discharge of 4000 $\text{m}^3 \text{s}^{-1}$ reached about 1800 m after 20 years, although in some locations the entire floodplain of about 5 km changed into braidplain. Also, sedimentation on the floodplain resulted in a local, larger, effective braidplain. A peak discharge of 2000 $\text{m}^3 \text{s}^{-1}$ resulted in an average width of about 1100 m, with minor effect of floodplain sedimentation. The reach-averaged braidplain widening was about 190% in 20 years for the 4000 $\text{m}^3 \text{s}^{-1}$ peak discharge scenario, about 140% for the 3000 $\text{m}^3 \text{s}^{-1}$ peak discharge scenario and about 110% for the 2000 $\text{m}^3 \text{s}^{-1}$ peak discharge scenario. The channel widening mainly occurred through chute channel formation.

The formation of chute channels on the floodplains in the simulation with a peak discharge of 4000 $\text{m}^3 \text{s}^{-1}$ is given in more detail in Figure 11. The flow velocity on the floodplains during the peak discharge was initially about 0.6–0.8 m s^{-1} with a water depth of about 40–80 cm. This situation resulted in avulsive channels on the floodplain at the locations where flow entered the floodplains (feature B in Figure 11) and head-cutting channels where the flow left the floodplains (feature A in Figure 11). After about 10–15 years, both type of channels were connected and formed chute chan-

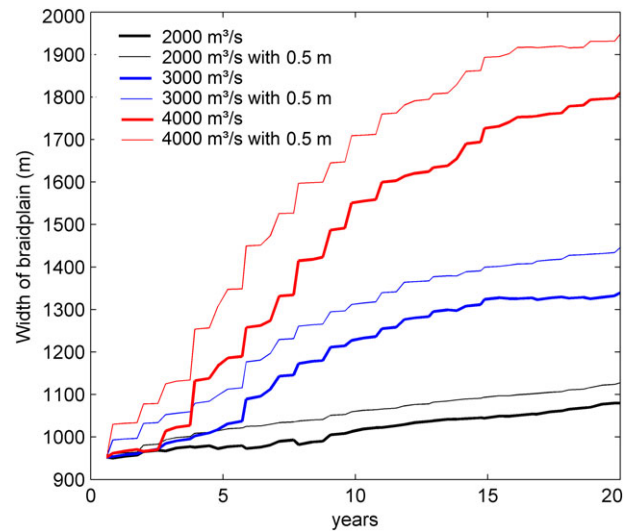


Figure 10. Reach-averaged width of the modelled braidplain for different peak discharge scenarios (bold lines). Also, the braidplain width in locations with floodplain sedimentation larger than 0.5 m is considered to be braidplain (thin lines). [Colour figure can be viewed at wileyonlinelibrary.com]

nels. Some of these chute channels eventually became the dominant channel branches (Figure 11f).

To recapitulate, the model results showed that the channel pattern and dynamics were strongly affected by the peak discharge. Within the main channel, the mid-channel bars and bank-attached bars were larger and higher for larger peak discharge. On the floodplains, a higher peak discharge resulted in more flow over the floodplains, and the formation of avulsive channels and head-cutting channels, resulting in a higher braiding intensity.

Non-uniform bed roughness

In the future scenarios, we applied a constant and uniform C (Eqs. (1), (2), (4) and (6)). This procedure means that the main channel and floodplains have the same roughness. It also means that the floodplains receive a relatively low Manning's n or Nikuradse k_s bed roughness when we convert from the uniform C , because of the relatively small water depth on the floodplains. However, the bed roughness on the floodplains should be higher than in the channel due to vegetation, human-induced obstructions and other irregularities. Therefore, we conducted a test run with a constant, uniform Nikuradse k_s value, which accounts for water depth and gives a low Chézy roughness C in shallow areas such as the floodplains (Eq. (11)). The Nikuradse k_s was set to 0.15 m, which fits with a C of 45 $\text{m}^{0.5} \text{s}^{-1}$ for a water depth of 4 m, equal to the initial depth of the channel.

The resulting BI is shown in Figure 9. The BI for the uniform k_s is about 0.5 higher than the BI for the uniform C roughness. Also, the uniform k_s results in more sedimentation on the bars and floodplains, and, as a result, higher surface levels of the bars and floodplains. An explanation for these higher BI and surface levels is that a uniform k_s value gives a higher overall bed roughness, and therefore a steeper downstream energy gradient. Taking into account an equal downstream water level, the steeper gradient results in higher peak water levels, and more space for sedimentation on the bars and floodplains. Also, compared to the uniform C , the uniform k_s gives a larger deviation in flow velocity between the shallow and deep water areas, which stimulates channel formation.

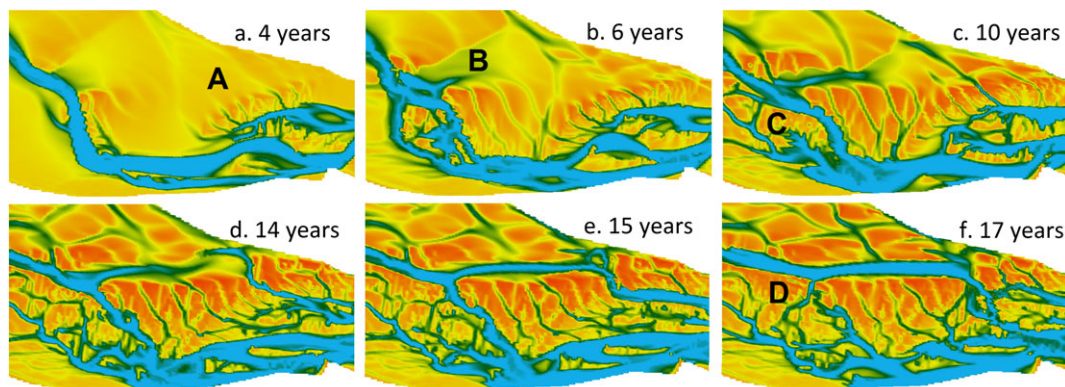


Figure 11. Example of the initiation and development of chute channels on the floodplains in the case of a peak discharge of $4000 \text{ m}^3 \text{ s}^{-1}$. Head-cutting channels are formed where flow from the floodplains flows back into the main channel (A). At the same time, avulsive channels are formed by flow from the main channel to the floodplains (B). When the head-cutting and avulsive channels meet, the chute channel attracts most discharge and becomes dominant. At the same time, other bifurcations become unstable and branches close (C, D). [Colour figure can be viewed at wileyonlinelibrary.com]

Alternative discharge regulation schemes

Furthermore, we can consider the duration of the peak discharge, and try alternative discharge regulation scenarios that deviate from the single month of peak discharge. For example, 2 months with a constant $2000 \text{ m}^3 \text{ s}^{-1}$ peak discharge could be an alternative for 1 month of $4000 \text{ m}^3 \text{ s}^{-1}$. Also, a peak discharge of $4000 \text{ m}^3 \text{ s}^{-1}$ for half a month could be an alternative for 1 month of $2000 \text{ m}^3 \text{ s}^{-1}$. The results of these two alternative scenarios are given in Figure 9.

The results showed that 2 months of $2000 \text{ m}^3 \text{ s}^{-1}$ gave a BI of about 3.0, which was lower than the 4.0 for 1 month of $4000 \text{ m}^3 \text{ s}^{-1}$. An explanation for this is the higher peak water level in the latter case that enabled significant flow over the floodplains and initiation of chute channels on the floodplains. At the same time, the 2 months of $2000 \text{ m}^3 \text{ s}^{-1}$ gave a 0.5 higher BI than a single month of $2000 \text{ m}^3 \text{ s}^{-1}$, which shows that a longer peak discharge period results in a higher degree of braiding. Comparison between the single month of $2000 \text{ m}^3 \text{ s}^{-1}$ and a half month of $4000 \text{ m}^3 \text{ s}^{-1}$ resulted in a similar pattern: the model run with half a month of $4000 \text{ m}^3 \text{ s}^{-1}$ peak discharge gave a higher BI than a peak discharge of $2000 \text{ m}^3 \text{ s}^{-1}$ and a duration of 1 month.

Discussion

This study aimed to give insight into the morphological response of a braiding river reach to an increase in annual peak discharges. Numerical modelling was conducted to construct 'data sets' of the morphological evolution in the study reach. In this discussion, we elaborate on these results and their implications. First, we discuss the modelling of the study reach, followed by the changes in channel pattern and dynamics predicted in the model, and the implications for the management of discharge regulation in the Upper Yellow River.

Impact of higher peak discharges

The model results gave a clear and consistent picture of the possible effects of higher peak discharges on the morphodynamics and channel planform in the braiding study reach. In general, an increase in peak discharge resulted in an increase in braiding intensity. This outcome is consistent with the findings of Richard and Julien (2003), Egozi and Ashmore (2009), Nones *et al.* (2013) and others. However, it also requires a

discussion about the transition from the situation with the original discharge regime and the later situation with the new discharge regime.

In the transition, channel widening by bank erosion was expected to be a major process, based on hydraulic geometry relations, but appeared to be a minor process. The formation of new mid-channel bars was also a minor process, at least when comparing the situation with the original discharge regime and the later situation with new discharge regime. It is likely that mid-channel bar formation is more important if major channel widening occurs after a discharge increase, because of the larger width–depth ratio. Instead, the dominant impact of the new discharge regime appeared to be the formation of chute channels on the floodplains. The chute channels developed in our simulations with high peak discharge were similar to the chute channels described by Smith and Pearce (2002), Van Dijk and Schuurman (2014) and others. They showed the formation of chute channels by flow rerouting over the floodplains. This process started with scour where flow leaves the main channel and with backward-migrating secondary channel erosion where flow returns to the main channel, similar to what occurred in the simulations of the Upper Yellow River.

The increase in peak discharge gave a significant change in channel pattern and transformed large parts of the floodplains into islands and channels. The loss of valuable land on the floodplains by the channel widening and chute channels is socially and economically undesirable. However, elevated land surface, vegetation and numerous kinds of structures in the floodplains might limit the formation of chute channels on the floodplains (Van Dijk and Schuurman, 2014; van Oorschot *et al.*, 2016) and thus reduce the impact of higher peak discharges. For example, flood protection and elevated roads may (partly) block the flow over the floodplains. Future boundary conditions (rainfall and discharge) and human-induced disturbances (dredging, agriculture, dykes and other engineering structures, water extraction) are not known, which imposes a limitation on the predictability of the natural developments. We worked with scenarios, and models helped in predicting a trend rather than giving an exact answer.

Also, the effects of sediment storage in the upstream hydropower reservoirs and flushing of sediment from the hydropower reservoirs were not simulated. One reason for this was the large distance between the large hydropower reservoirs and the study site, which was assumed to be sufficient to reach equilibrium conditions at the study site. Nevertheless, non-equilibrium conditions, in our case a deficiency of sediment released from the hydropower reservoirs, is expected to result in river bed degradation and increased bank erosion

rates, starting near the hydropower dam. In the long term, it might adjust the large-scale river slope, which occurs at a timescale well beyond the 25 years simulated in this study.

Modelling of planform changes in braiding rivers

The main reason for applying numerical modelling in this study was the ability of a model to generate channel patterns and dynamics based on user-defined initial conditions, boundary conditions and other settings. Conducting scenario analysis is relatively easy by varying one input parameter and by determining the differences in model results. In this way, the effect of input parameters can be isolated, which is difficult and often impossible in field measurements. The same approach has been used by, among others, Crosato *et al.* (2012), Nicholas (2013a) and Schuurman *et al.* (2013).

The general bar pattern in the braiding reach, described by the BI, was reproduced well. The channel pattern was found to be sensitive to the input parameters, especially the bed slope effect. This outcome is in agreement with Schuurman *et al.* (2013), for example, and affirms the necessity for improvement of the bed slope effect parametrization. The median grain size, on the other hand, had a relatively small effect on the channel pattern. The BI was slightly reduced for larger grain size, which is in agreement with the literature (Kleinhans and Van den Berg, 2011). The relatively small effect of the grain size suggests that the relatively large grain size of the desert sand along the study reach also has a relatively minor effect on the channel pattern.

Also, this study confirmed the value of numerical models, because the model showed the adaptation of the study reach to the new discharge regime, including the intermediate stages and processes involved with it. The model simulations gave insight into the channel dynamics leading to a new dynamic equilibrium channel pattern, with the distinct responses of bars, channel branches and floodplain. This exercise is a valuable addition to the classical end-member predictors, such as analytical methods, hydraulic geometry relations and channel pattern diagrams.

One of the complicated processes to model was the lateral shift of channel branches, as described by Yao *et al.* (2011), for example. We found that a boost in the spiral flow in combination with a boost in the transverse bed slope effect resulted in relatively high rates of lateral channel shift and prevented a static pattern of bar and channel branches, which occurred in the simulations of Schuurman *et al.* (2013). The wet–dry bank erosion algorithm in the model was unable to retain channel dynamics, which was also found by Stecca *et al.* (2017), and calls for a more sophisticated physics-based bank erosion algorithm in the model (Williams *et al.*, 2016). The difficulty of modelling lateral channel shift is, however, not unique to Delft3D, and physics-based numerical models that do contain a more sophisticated bank erosion routine often have other significant deficiencies, for example their applicability only to flume-scale channels (e.g. Duan and Julien, 2010; Asahi *et al.*, 2013) or cross-sectional profiles (Stecca *et al.*, 2017), or they produce questionable bar shapes (see Schuurman *et al.*, 2016b, for discussion). The present results strongly suggest that the local, detailed processes that lead to a conversion from channels and bars to floodplain, and to floodplain destruction by channel migration and avulsion, are important for reach-scale morphology and dynamics in braided rivers, not merely for meandering rivers where this has long been known to be important (Kleinhans and Van den Berg, 2011; Schuurman *et al.*, 2016b).

Conclusions

In this study we used numerical modelling to estimate the effects of higher peak discharges on the channel pattern and the dynamics of bars, floodplain and channel branches in a braided reach of the Upper Yellow River. The model gave a consistent picture, with the formation of new channel branches in the floodplains as the primary process following the increase of peak discharge. Due to these chute channels, the width of the braidplain increased significantly in the case of higher peak discharges.

Compared to the impact of chute channels in the floodplains on the width of the braidplain, channel widening by bank erosion was found to be a minor process. In addition to the floodplain-related processes, an increase in peak discharges resulted in larger mid-channel bars in the main channel. Overall, higher peak discharges increased the braiding intensity and transformed a mildly braiding river reach to a highly braiding river reach.

In this study, ongoing channel dynamics were achieved by boosting both the spiral flow and the bed slope effect, a combination that accelerated bank erosion along the floodplains and along the islands. This outcome shows that the local-scale processes determining channel–floodplain conversion and floodplain destruction have reach-scale effects on the braided river. It also demonstrates the need for physics-based methods for bank erosion modelling.

Acknowledgements— This research is funded by the National Basic Research Program of China (No. 2011CB403302). We are grateful to Paul Carling and an anonymous reviewer for providing constructive comments to improve this article.

References

- Ahktar MP, Sharma N, Ojha CSP. 2011. Braiding process and bank erosion in the Brahmaputra River. *International Journal of Sediment Research* **26**(4): 431–444.
- Asahi K, Shimizu Y, Nelson J, Parker G. 2013. Numerical simulation of river meandering with self-evolving banks. *Journal of Geophysical Research* **118**(4): 2208–2229.
- Ashworth JP, Best JL, Roden JE, Bristow CS, Klaassen GJ. 2000. Morphological evolution and dynamics of a large, sand braid-bar, Jamuna River, Bangladesh. *Sedimentology* **47**(3): 533–555.
- Baki ABM, Gan TY. 2012. Riverbank migration and island dynamics of the braided Jamuna River of the Ganges–Brahmaputra basin using multi-temporal Landsat images. *Quaternary International* **263**: 148–161.
- Bertoldi W, Siviglia A, Tettamanti S, Toffolon M, Vetsch D, Francalanci S. 2014. Modeling vegetation controls on fluvial morphological trajectories. *Geophysical Research Letters* **41**: 7167–7175.
- Bridge JS. 2003. *Rivers and Floodplains: Forms, Processes and Sedimentary Record*. Blackwell: Oxford, UK.
- Crosato A, Mosselman E. 2009. Simple physics-based predictor for the number of river bars and the transition between meandering and braiding. *Water Resources Research* **45**: W03424. <https://doi.org/10.1029/2008WR007242>.
- Crosato A, Saleh MS. 2010. Numerical study on the effects of floodplain vegetation on river planform style. *Earth Surface Processes and Landforms* **36**(6): 711–720.
- Crosato A, Mosselman E, Desta FB, Uijttewaals WSJ. 2011. Experimental and numerical evidence for intrinsic nonmigrating bars in alluvial channels. *Water Resources Research* **47**: W03511. <https://doi.org/10.1029/2010WR009714>.
- Crosato A, Desta FB, Cornelisse J, Schuurman F, Uijttewaals WSJ. 2012. Experimental and numerical findings on the long-term evolution of migrating alternate bars in alluvial channels. *Water Resources Research* **48**: W06524. <https://doi.org/10.1029/2011WR011320>.

- Deltares. 2009. *Delft3D-FLOW User Manual: Simulation of Multi-Dimensional Hydrodynamic Flows and Transport Phenomena, Including Sediments*. Deltares: Delft.
- Du HQ, Xue X, Wang T. 2014. Estimation of the quantity of aeolian saltation sediments blown into the Yellow River from the Ulanbuh Desert, China. *Journal of Arid Land* **6**(2): 205–218.
- Duan JG, Julien PY. 2010. Numerical simulation of meandering evolution. *Journal of Hydrology* **391**(1–2): 34–46.
- Egozi R, Ashmore P. 2009. Experimental analysis of braided channel pattern response to increased discharge. *Journal of Geophysical Research* **114**: F02012. <https://doi.org/10.1029/2008JF001099>.
- Engelund F, Hansen E. 1967. *A Monograph on Sediment Transport in Alluvial Streams*. Teknisk: Copenhagen, Denmark.
- Engelund F, Skovgaard O. 1973. On the origin of meandering and braiding in alluvial streams. *Journal of Fluid Mechanics* **57**: 280–302.
- Fredsoe J. 1978. Meandering and braiding of rivers. *Journal of Fluid Mechanics* **84**(4): 609–624.
- Ikeda S, Nishimura T. 1986. Flow and bed profile in meandering sand-silt rivers. *Journal of Hydraulic Engineering* **112**(7): 562–579.
- Klaassen GJ, 1992 Masselink G. *Planform changes of a braided river with fine sand as bed and bank material*, In 5th International Symposium on River Sedimentation. Karlsruhe, Germany, 459–471.
- Kleinmans MG, Bierkens MFP, Van der Perk M. 2010. On the use of laboratory experimentation: 'Hydrologists, bring out shovels and garden hoses and hit the dirt'. *Hydrology and Earth System Sciences* **14**(2): 369–382.
- Kleinmans MG, Van den Berg JH. 2011. River channel and bar patterns explained and predicted by an empirical and a physics-based method. *Earth Surface Processes and Landforms* **36**(6): 721–738.
- Koch FG, Flokstra C. 1981. Bed level computations for curved alluvial channels, In *Proceedings of the XIX Congress of the International Association for Hydraulic Research*, Vol. 2: New Delhi, India, 357.
- Latrubesse EM. 2008. Patterns of anabranching channels: the ultimate end-member adjustment of mega rivers. *Geomorphology* **101**(1–2): 130–145.
- Leopold LB, Maddock T. 1953. *The hydraulic geometry of stream channels and some physiographic implications*. Professional Paper 252, US Geological Survey, Washington, DC.
- Leopold LB, Wolman MG. 1957. River channel patterns: braided, meandering and straight. Professional Paper 282B, US Geological Survey, Washington, DC; 39–85.
- Lesser GR, Roelvink JA, Kester J A TMV, Stelling GS. 2004. Development and validation of a three-dimensional morphological model. *Coastal Engineering* **51**(8–9): 883–915.
- Lewin J, Ashworth PJ, Strick RJP. 2016. Spillage sedimentation on large river floodplains. *Earth Surface Processes and Landforms* **42**(2): 290–305.
- Lischan R, Suiji W, Xiaoli F. 2010. Channel change at Toudaoguai Station and its responses to the operation of upstream reservoirs in the upper Yellow River. *Journal of Geographical Sciences* **20**(2): 231–247.
- Ma Y, Huang HQ, Nanson GC, Li Y, Yao W. 2012. Channel adjustment in response to the operation of large dams: the upper reach of the lower Yellow River. *Geomorphology* **147**(148): 35–48.
- Nanson G, Knighton A. 1996. Anabranching rivers: their cause, character and classification. *Earth Surface Processes and Landforms* **21**(3): 217–239.
- Nicholas AP. 2013a. Modelling the continuum of river channel patterns. *Earth Surface Processes and Landforms* **38**(10): 1187–1196.
- Nicholas AP. 2013b. Morphodynamic diversity of the world's largest rivers. *Geology* **41**(4): 475–478.
- Nones M, Ronco P, Di Silvio G. 2013. Modelling the impact of large impoundments on the Lower Zambezi River. *International Journal of River Basin Management* **11**(2): 221–236.
- Parker G, Seminara G, Solari L. 2003. Bed load at low Shields stress on arbitrarily sloping beds: alternative entrainment formulation. *Water Resources Research* **39**(7): 1183.
- Parker G, Wilcock PR, Paola C, Dietrich WE, Pitlick J. 2007. Physical basis for quasi-universal relations describing bankfull hydraulic geometry of single-thread gravel bed rivers. *Journal of Geophysical Research* **112**(F4): 2156–2202.
- Rice SP, Church M, Wooldbridge CL, Hickin EJ. 2009. Morphology and evolution of bars in a wandering gravel-bed river: lower Fraser river, British Columbia, Canada. *Sedimentology* **56**(3): 709–736.
- Richard G, Julien P. 2003. Dam impacts on and restoration of an alluvial river: Rio Grande, New Mexico. *International Journal of Sediment Research* **18**(2): 89–96.
- Roelvink JA. 2006. Coastal morphodynamic evolution techniques. *Coastal Engineering* **53**(2–3): 277–287.
- Schuurman F, Kleinmans MG. 2015. Bar dynamics and bifurcation evolution in a modelled braided sand-bed river. *Earth Surface Processes and Landforms* **40**: 1318–1333.
- Schuurman F, Kleinmans MG, Marra WA. 2013. Physics-based modeling of large braided sand-bed rivers: bar pattern formation, dynamics, and sensitivity. *Journal of Geophysical Research* **118**(4): 2509–2527.
- Schuurman F, Kleinmans MG, Middelkoop H. 2016a. Network response to disturbances in large sand-bed braided rivers. *Earth Surface Dynamics* **4**: 25–45.
- Schuurman F, Shimizu Y, Iwasaki T, Kleinmans MG. 2016b. Dynamic meandering in response to upstream perturbations and floodplain formation. *Geomorphology* **253**: 94–109.
- Smith DG, Pearce CM. 2002. Ice jam-caused fluvial gullies and scour holes on northern river flood plains. *Geomorphology* **42**(1–2): 85–95.
- South-to-North Water Diversion Project Construction Committee. 2016. The South-to-North Water Diversion Project. *Engineering* **2**(3): 265–267.
- Stecca G, Measures R, Hicks M. 2017. A framework for the analysis of noncohesive bank erosion algorithms in morphodynamic modeling. *Water Resources Research* **53**(8): 6663–6686.
- Struiksma N, Olesen K, Flokstra C, De Vriend H. 1985. Bed deformation in curved alluvial channels. *Journal of Hydraulic Research* **23**(1): 57–79.
- Sun J, Lin B, Yang H. 2015. Development and application of a braided river model with non-uniform sediment transport. *Water Resources Research* **81**: 62–74.
- Ta W, Yang G, Qu J, Wang T, Dai F. 2003. The effect of the coarse aeolian sand on siltation of the Inner Mongolian Reach of the Yellow River. *Environmental Geology* **43**(5): 493–502.
- Ta W, Xiao H, Dong Z. 2008. Long-term morphodynamic changes of a desert reach of the Yellow River following upstream large reservoirs' operation. *Geomorphology* **97**(3–4): 249–259.
- Ta W, Wang H, Jia X. 2011. Downstream fining in contrasting reaches of the sand-bedded Yellow River. *Hydrological Processes* **25**(24): 3693–3700.
- Talmon AM, Struiksma N, Van Mierlo M CLM. 1995. Laboratory measurements of the direction of sediment transport on transverse alluvial-bed slopes. *Journal of Hydraulic Research* **33**(4): 495–517.
- Thorne CR, Russel APG, Alam MK. 1993. Planform pattern and channel evolution of the Brahmaputra River, Bangladesh. In *Braided Rivers*, Best J L, Bristow C S (eds), Geological Society: London; 257–276.
- Van der Wegen M, Roelvink JA. 2008. Long-term morphodynamic evolution of a tidal embayment using a two-dimensional, process-based model. *Journal of Geophysical Research* **113**: C03016.
- Van Dijk WM, Schuurman F. 2014. Bifurcation instability and chute cutoff development in meandering gravel-bed rivers. *Geomorphology* **213**: 277–291.
- van Oorschot M, Kleinmans MG, Geerling GJ, Middelkoop H. 2016. Distinct patterns of interaction between vegetation and morphodynamics. *Earth Surface Processes and Landforms* **41**(6): 791–808.
- Vesipa R, Camporeale C, Ridolfi L. 2015. Noise-driven cooperative dynamics between vegetation and topography in riparian zones. *Geophysical Research Letters* **42**: 8021–8030.
- Wang H, Yang Z, Saito Y, Liu JP, Sun X, Wang Y. 2007. Stepwise decrease of the Huanghe (Yellow River) sediment load (1950–2005): impacts of climate change and human activities. *Global and Planetary Change* **57**(3–4): 331–354.
- Wang H, Jia X, Peng W. 2015. Selective deposition response to aeolian-fluvial sediment supply in the desert braided channel of the upper Yellow River, China. *Natural Hazards and Earth System Sciences* **15**(9): 1955–1962.

- Webber M, Crow-Miller B, Rogers S. 2017. The South–North Water Transfer Project: remaking the geography of China. *Regional Studies* **51**(3): 370–382.
- Wheaton JM, Brasington J, Darby SE, Kasprak A. 2013. Morphodynamic signatures of braiding mechanisms as expressed through change in sediment storage in a gravel-bed river. *Journal of Geophysical Research* **118**(2): 759–779.
- Williams RD, Brasington J, Hicks DM, Measures R, Rennie CD, Vericat D. 2013. Hydraulic validation of two-dimensional simulations of braided river flow with spatially continuous aDcp data. *Water Resources Research* **49**(9): 5183–5205.
- Williams RD, Measures R, Hicks DM, Brasington J. 2016. Assessment of a numerical model to reproduce event-scale erosion and deposition distributions in a braided river. *Water Resources Research* **52**(8): 6621–6642.
- Xu D, Bai Y, Ma J, Tan Y. 2009. Response of the hydrological regime of the Yellow River to the changing monsoon intensity and human activity. *Hydrological Sciences Journal* **54**(1): 90–100.
- Yang H, Lin B, Zhou J. 2015. Physics-based numerical modelling of large braided rivers dominated by suspended sediment. *Hydrological Processes* **29**(8): 1925–1941.
- Yao Z, Ta W, Jia X, Xiao J. 2011. Bank erosion and accretion along the Ningxia–Inner Mongolia reaches of the Yellow River from 1958 to 2008. *Geomorphology* **127**(1–2): 99–106.

Supporting Information

Additional supporting information may be found online in the supporting information tab for this article.